Journal of Inorganic and Organometallic Polymers and Materials
https://doi.org/10.1007/s10904-024-03024-4

RESEARCH

Mg^{2+} Doped ZCFAO Spinel Ferrite: Structural, Optical, Dielectric and Magnetic Explorations

A. M. Moustafa[1,2] · S. A. Gad[1,2] · H. M. Hashem[1,2]

Received: 27 December 2023 / Accepted: 30 January 2024

Abstract
A series of Mg doped ZCFAO ($Zn_{0.3-x}Mg_xCu_{0.7}Al_{0.3}Fe_{1.7}O_4$ ($0.05 \leq x \leq 0.25$) spinel samples were synthesized by solid state reaction method. XRD, was utilized to investigate the structure phase, microstructural characteristics, The optical properties were analyzed; Biological instruments Sp-150 potentiostate is employed to investigate the dielectric measurements in the frequency range of 10 Hz to 1 MHz at various temperatures from 300 to 650 K. Vibrating sample magnetometer VSM was employed to examine the magnetic characteristics in the applied magnetic field ranging from − 20 to 20 kG. The creation of a single-phase cubic spinel was validated by X-ray analysis. The leverage of replacing Zn by Mg leads to enhancement in the lattice parameters, reducing both of the degree of inversion, crystal distortion and compelled these samples to be normal spinel. It turned out that as the degree of inversion sank, the crystallite size declined. The values of dislocations density was found in the order of 10^{-5} which reveal improving and completing the crystallization of the ferrite samples. The samples have an optical energy gap in the range 3.1–3.38 eV, according to the inferred optical characteristics. The dielectric constant revealed the normal behavior of spinel ferrite it decreases with increasing frequency and enhanced with increasing temperature. It seems that the microstructure of the compound consists of both high-conductive grains and low-conductive grain boundaries, which has been confirmed by the complex impedance. Additionally, the presence of the Maxwell–Wagner relaxation process is also detected. This information can provide valuable insights into the properties and behavior of the compound. Using Nyquist plot, the sample impedance characteristics were interpreted while taking grain and grain boundary contributions into account. The magnetic properties proved that doping ZCFAO with diamagnetic cations (Mg) increases both of saturation magnetization from 16.416 up to 29.983 emu/g and the magnetocrystalline anisotropic constant from 1319.24 to 1612.804 because the two main factors that influence the magnetic properties are the distribution of cations between the octahedral and tetrahedral sites and the magnetic moment of each of its cations. Novelty of our work replacing Zn by Mg (both of them diamagnetic materials) enhance the magnetic properties. Synthesized materials may reexamine the mechanisms underlying Mg^{2+} induced cationic exchange in ZCFAO and have prospective uses as soft-magnetic materials.

Keywords Ferrite · X-ray crystallography · Optical properties · Dielectric properties · Magnetic properties

1 Introduction

Commercial electronics applications have increased tremendously over the past few decades as a result of the discovery of several particularly important ferrite materials. There is a demand for electronic devices that are more compact, economical, and effective due to the rapid growth and development of telecommunications and information technology. Numerous functionalities are offered by electronic devices to simplify our lives [1].

Due to its fascinating electrical, optical, magnetic, and dielectric properties, spinel ferrites play a crucial role in the development of electronic devices. Additionally, ferrites are utilized in a wide range of innovative uses, including gas sensors, optoelectronics, transformer cores, transducers, magnetic hyperthermia, smart grids, magnetic resonance imaging, pigments, motors, inductors, radar, telecommunications [2] and microwave absorbers as well as energy storage.

✉ A. M. Moustafa
aishamoustafa@yahoo.com

[1] Solid State Physics Department, Physics Research Institute, National Research Centre, 33 El-Bohouth St., Dokki, Giza 12622, Egypt

[2] Physics Department, Faculty of Science, Helwan University, Helwan, Egypt

Published online: 11 April 2024

Spinel ferrites have been used in isolators, phase shifters, circulators, supercapacitors, and solar cells, among other energy storage and high-frequency devices [3–7].These spinels typically contain divalent metal and trivalent cations at the A-site and B-site of the unit cells, respectively [8, 9]. The cubic unit cell has 64 tetrahedral [A-site] and 32 octahedral [B-site] interstices. The material under consideration has 16 cations and 32 [B-site] octahedral interstices. The unit cell, which contains eight formula units ($M_8Fe_{16}O_{32}$), is characterized by the distribution of cations across the available interstices. Specifically, half of the 32 octahedral interstices are occupied by 16 cations, while the remaining eight cations occupy one-eighth of the 64 tetrahedral interstices. Moreover, the structure contains 32 oxygen atoms arranged in a densely packed face-centered cubic configuration. Cations will be able to freely move across the sites in a unit cell because to the 72 open interstices [9]. It's interesting to note that the properties and applications of ferrites are influenced by various factors, such as microstructure, grain size, cation distribution in lattices, and synthesis method. It's important to take these factors into consideration when studying or working with ferrites.

The mixed valence cations, on the other hand, are formulated in two distinct crystallographic sub-lattices and are, respectively, represented by $A[B]_2O_4$ and $B[AB]O_4$. When it comes to oxygen ions, the cations allocate inside the bracket have octahedral coordination, whereas those assigned outside the bracket have tetrahedral coordination [10]. For spinels to be used effectively in applications for electronic devices, their electrical and electrochemical properties are significantly influenced by these crystallographic sub-lattice compositions. [11, 12]. Spinel ferrites have a wide range of possible applications and a well-established market. Researchers, scientists, and engineers have been fascinated by various bulk and nanoscale ferrite materials for more than 50 years. The characteristics of ferrites can be changed by manipulating various factors such as exchanging or adding 2+ (divalent) or 3+ (trivalent) ions, modifying the synthesis procedure, and regulating both the duration and the temperature of sintering. This information comes from Ref. [13]. Among the important spinel ferrites MFe_2O_4, copper ferrite ($CuFe_2O_4$) is notable for its intriguing magnetic and electrical properties with chemical and thermal stabilities, as well as its phase transitions, electrical switching, phase changes, and variation in tetragonality under various conditions [14]. Magneto-optic recording devices with high density, gas sensing [15], catalytic applications [16–18], Li-ion batteries [19], color imaging, bioprocessing, magnetic refrigeration, and ferrofluids [13, 20] are only a few of the many uses for it.

Furthermore, $CuFe_2O_4$ assumes significant importance due to its high thermal stability, high electric conductivity, and elevated catalytic activity for O_2 evolution from the alumina-cryolite system utilized to produce aluminum [21]. The versatility of $CuFe_2O_4$'s structural morphologies has also made it a significant ferrite. It is known that tetragonal and cubic forms of $CuFe_2O_4$ occur. The cubic structure has more Cu^{2+} ions in the tetrahedral interstitial locations than in the octahedral ones, while Fe^{3+} fills the remaining interstitial places to form a mixed spinel ferrite. The tetragonal structure with a lattice parameter ratio of roughly 1.06 when subjected to gradual cooling. Cu^{2+} ions nearly exclusively occupy the octahedral sublattice in the tetragonal phase of Cu–ferrite, whereas Fe^{3+} ions are evenly distributed throughout the tetrahedral and octahedral sublattices [22]. The tetragonal structure is stable at room temperature because of Jahn–Teller distortion, and it changed to the cubic phase at temperatures of 360 °C and higher. The magnetic characteristics have a direct impact on the distortion. The cubic structure has a bigger surface area.

Although nanocrystalline copper ferrite exhibits unique photocatalytic characteristics, its narrow bandgap causes a high rate of photogenerated electron (e^-) and hole (h^+) recombination. The study of Abuilaiwia et al [23] demonstrates that doping $CuFe_{2-x}Al_xO_4$ ($0 \le x \le 1$) nanoparticles produced by a solid-state, mechanochemical process with Al^{3+} reduces the (e^-/h^+) recombination rate and increases the availability of charge carriers through. Al^{3+} doping lowers the lattice parameter because the smaller ionic radius of Al^{3+} ions replace the larger ionic radius of Fe^{3+} ions. On the other hand, Al^{3+} doped samples show more sintering and larger crystallite sizes. A reduction in the photoluminescence signal, ascribed to the reduced rate of (e^-/h^+) recombination, demonstrates the impact of Al^{3+} doping on the optical characteristics of $CuFe_{2-x}Al_xO_4$ ($0 \le x \le 1$) nanoparticles. Al^{3+} doping hence lengthens the transition time and enhances the availability of charge carriers for possible photocatalytic uses.

Cu–Mg ferrites, of a series of $Cu_{1-x}Mg_xFe_2O_4$ with (x = 0.2, 0.4, 0.6, 0.8, and 1.0) synthesized by double sintering ceramic method at 1150 °C, were examined structurally, magnetically, and electrically by Shahida Akhter et al. [24]. The creation of a single-phase cubic spinel was validated by X-ray analysis, and it was discovered that the grain size and lattice parameters decreased as the Mg concentration increased. With an increase in Mg concentration, the real part of initial permeability (μ′) decreases, possibly due to smaller grains. Additionally, they discovered that AC resistivity decreased with frequency, showing typical ferrimagnetic behavior. Shahida Akhter et al. [25] studied the Zn substituted Cu–Zn ferrites have been created using the conventional double sintering ceramic technique at 950 °C for 4 h. The single phase of a pure cubic spinel structure is indicated via structural analysis. The lattice constant increases linearly as the Zn concentration increases and follows Vegard's law because Zn^{2+} and Cu^{2+}

have different ionic radii. Zinc appears to be aiding in the densification of the materials because the X-ray and bulk densities of the Cu–Zn ferrite are dramatically reduced while porosity increases and SEM micrographs show a diminution in grain size with an increase in Zn content,. When Zn content increases up to x = 0.5, the real part of initial permeability, μ′, increases; and beyond that point, it decreases.

Sumi Akter et al. [26] prepared a series of single phase $Cu_{0.5}Mg_{0.5}Cr_xFe_{2-x}O_4$ ($0.0 \le x \le 0.16$) using the sol–gel technique at 700 °C for 4 h. Images obtained with a FESEM show non-spherical particles and a surface shape that is almost uniform. It was discovered that the average grain size decreased as the Cr content rose. EDS spectroscopic analysis of the original composition and the instance doping sample (x = 0.08) showed that the sample contained doped Cr in addition to Fe, Mg, Cu, and O. The magnetic properties are significantly affected by Cr doping fluctuations. As the Cr level rises until x = 0.08, the saturation magnetization (Ms) decreases and then increases once more as the Cr concentration rises, this may be related to the rapid antiferromagnetic Cr departure from B sites. Permeability measurements also show a similar pattern. Considering that μ′ is correlated with both grain size and Ms squared, this is to be expected. As frequency increases, the imaginary component of the permeability drops and stays almost constant in the high frequency range. As frequency is increased, the dielectric constant falls and, at higher frequencies, practically stays constant. The dielectric permittivity increases with increasing Cr content up to x = 0.08.; however, as Cr concentrations rise, it falls. Lower hopping probabilities across grain boundaries may account for the descending trend of the dielectric measurement and growing resistivity with Cr doping beyond the x = 0.08 concentration. These samples have a low dielectric loss, making them ideal for use in high-frequency systems.

The current work's goals and objectives are to improve or (enhance) the magnetic properties via Mg doping to reduce the crystal distortion and redistribution of cations, in addition to investigating the optical and dielectric properties.

2 Experimental

The spinel series ZCFAO with the chemical formula $Zn_{0.3-x}Mg_xCu_{0.7}Al_{0.3}Fe_{1.7}O_4$ ($0.05 \le x \le 0.25$) produced over a 6-h period at 1000 °C via a solid state process. A prior publication [27–29] contains a full process of the preparation process. Diffuse reflection measurements were performed with a Jasco (V-570) spectrophotometer in the 600–1200 nm wavelength range. Measurements of the magnetic characteristics were conducted using a vibrating sample magnetometer, model 9600-1-VSM. Measurements of the dielectric were carried out on Biological instruments Sp-150 potentiostate.

3 Results and Discussion

3.1 X-ray Diffraction

Figure 1 depict the X-ray diffraction pattern of a series of Magnesium doped (ZCAFO) ferrite with the chemical formula $Zn_{0.3-x}Mg_xCu0_{.7}Al_{0.3}Fe_{1.7}O_4$ ($0.05 \le x \le 0.25$) prepared by the solid state reaction. By matching the samples with ICSD card number 98-003-7429, the peak indexing was completed. The produced materials' cubic single phase is confirmed by the elimination of oxide diffraction signals. Also from this figure it is clear that, the peaks width had narrowed and intensified, pointing to the removal of prevalent sources of strain such as point defects, grain boundaries, chemical heterogeneities,

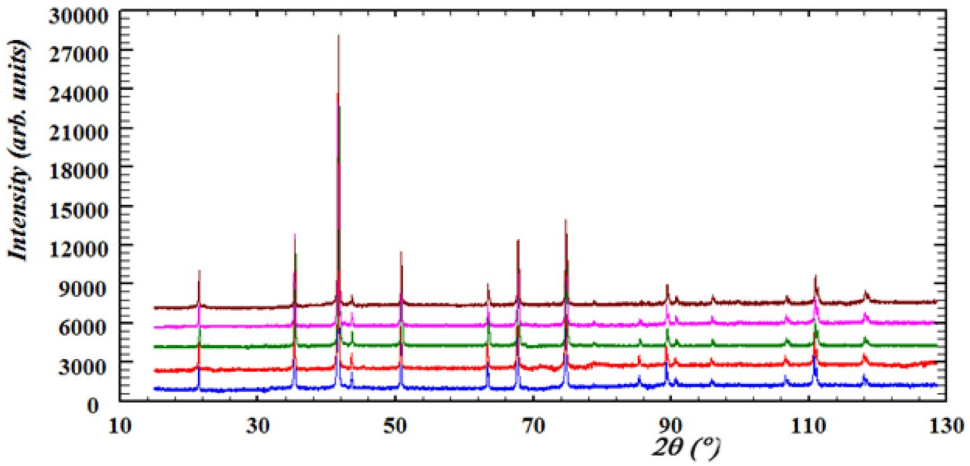

Fig. 1 Collected X-ray diffractogram for the Compounds $Zn_{0.3-x}Mg_xCu_{0.7}Al_{0.3}Fe_{1.7}O_4$ ($0.05 \le x \le 0.25$)

dislocations, stacking faults, and long-range internal stresses [30, 31]. Reference [32] contains a thorough explanation of the Rietveld refinement performed on the samples. For every prepared sample, the Rietveld refinement reveals the centrosymmetric structure of space group Fd-3m. With increasing Mg content the lattice parameters were found to decrease from 8.3494 to 8.3399 Å as a results of the (inequality or difference) between the ionic radius of Zn (0.74 Å) and magnesium (0.71 Å). Abuilaiwi et al. obtained the same behavior of decreasing the lattice parameters due to doping of copper ferrite by aluminum [23] The maximum degree of inversion was 0.5670 for Mg = 0.05 where the minimum was 0.1826 for Mg = 0.25 i.e. the increase in the magnesium content forced the structure of these samples to be normal spinel.

The crystallite size was found to decline as the degree of inversion decrease (Mg content increases), this result agrees with the results of decreasing the lattice parameters. The decrease in the crystallite size also may be due to the latent heat that had been trapped at the surface released, raising the local temperature and delaying development. The values of the dislocation density (δ) tabulated at Table 1 calculated from the equation:

$$\delta = 1/\mathrm{D} \tag{1}$$

Values of dislocations density in the order of 10^{-5} which reveal improving and completing the crystallization of the ferrite samples [33–35]. The specific surface area (S) was calculated using the relation [36, 37]:

$$\mathrm{S} = 6000/\mathrm{D}\rho_{\mathrm{m}}\mathrm{area}\ \left(\mathrm{m}^2\ \mathrm{g}^{-1}\right) \tag{2}$$

where D is the particle's diameter and ρ_m is the measured density. It is also clear from Table 1 that specific surface area (S) increases with decreasing the degree of inversion. The increment of S is a consequence of the declining crystallite size.

Table 1 The crystallite size, dislocation density, bulk density and specific surface area for the samples $Zn_{0.3-x}Mg_xCu_{0.7}Al_{0.3}Fe_{1.7}O_4$ ($0.05 \le x \le 0.25$)

Degree of inversion	Crystallite size (nm)	dislocation density (nm^{-2})	Bulk density	Specific surface area (m^2/g)
0.5670	157.3	4.0415E−05	3.9462	9.6659
0.4951	177.2	3.18473E−05	3.8936	8.6963
0.45	165.3	3.65977E−05	3.8163	9.5112
0.301	154.8	4.17309E−05	3.7632	10.2997
0.1826	134.5	5.52784E−05	3.7195	11.9935

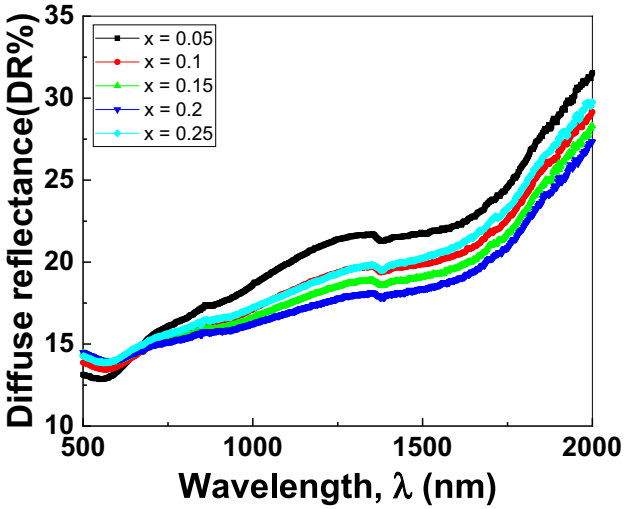

Fig. 2 The relation between the diffuse reflectance and wavelength

3.2 Optical Properties

Diffuse reflectance (DR) behavior of curves was found to be the same for five samples of ZCFAO; as shown in Fig. 2. The figure represents the relation between DR and wavelengths of the samples. It depicts the rise of DR with increasing wavelengths. The Kubelka–Munk equation is used to convert the reflectance spectra to the equivalent of absorption spectra [38]:

$$F(R) = \frac{(1-R)^2}{2R} \tag{3}$$

F(R) and R are the equivalent of the absorption coefficient and the reflectivity, respectively. The most important

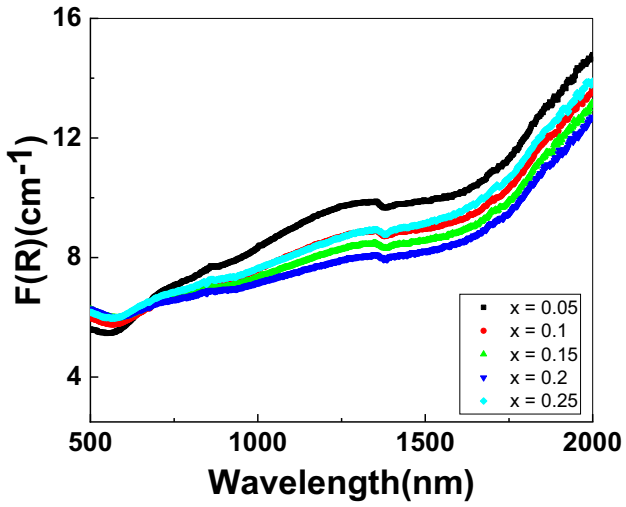

Fig. 3 F(R) vs. wavelength for $Zn_{0.3-x}Mg_xCu_{0.7}Al_{0.3}Fe_{1.7}O_4$ ($0.05 \le x \le 0.25$)

material property appropriate for optoelectronic applications is the optical band gap (E_g) [39]. The UV–Vis reflectance spectral data were used to calculate the optical energy band gaps of the samples based on Tauc's plots (Fig. 3) [40].

$$F(R) = \frac{B\left(h\nu - E_g\right)^n}{h\nu} = \alpha \tag{4}$$

where α is the absorption coefficient (α = (*R*)/d) and d is the thickness of the sample), hν is the incident photon energy (hν = 1240/wavelength), B is a constant which is related to the effective masses associated with the bands and E_g is the

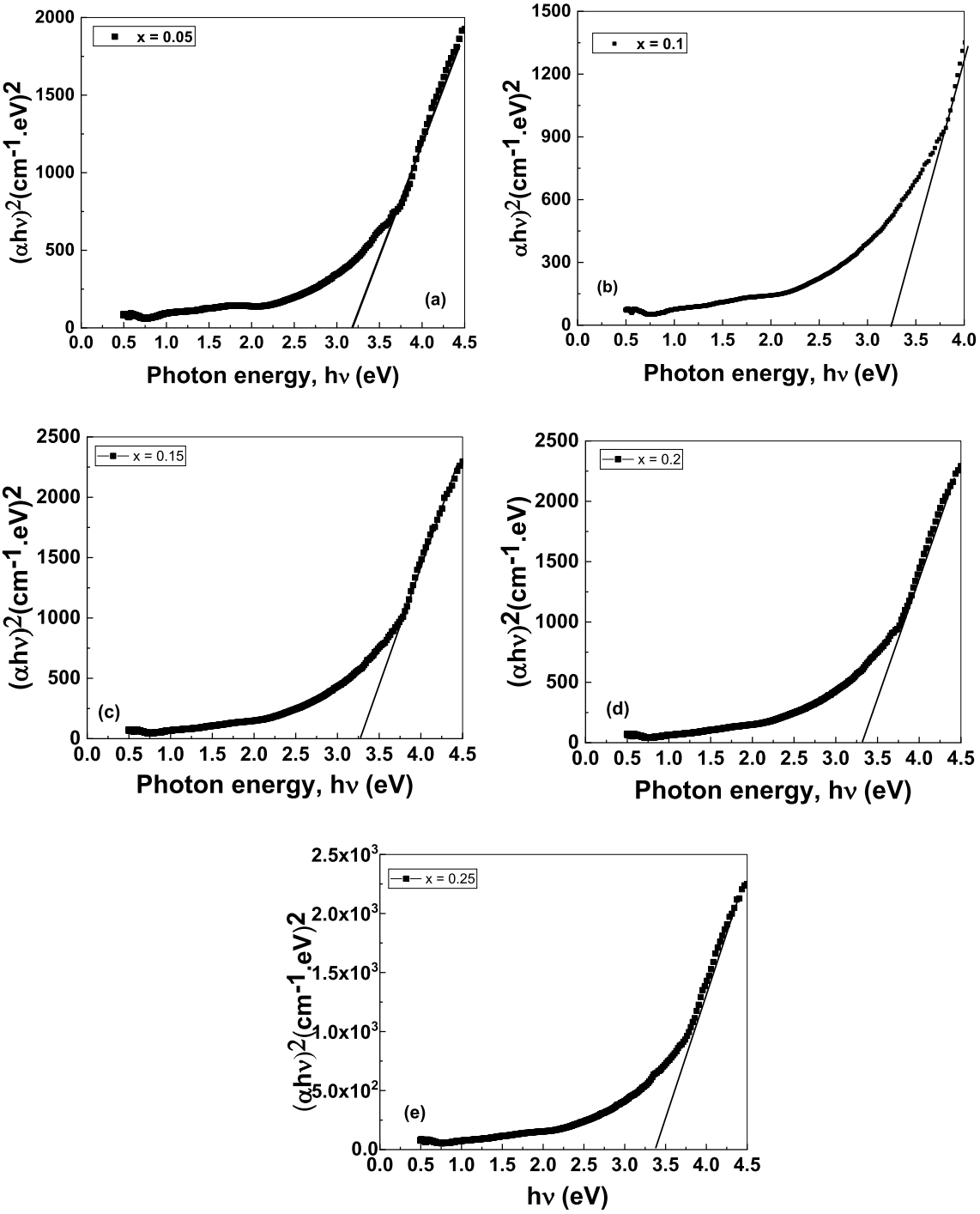

Fig. 4 **a**–**e** $(\alpha h\nu)^2$ against hν

electronic energy of the optical band gap. The optical band gap E_g of all samples was determined from the intercept of the linear portion of the curve $(\alpha h\nu)^2$ to y = 0 as shown in Fig. 4a–e. The optical band gap increases from 3.21 to 3.38 eV for the doped ZCFAO. The decrease in the crystallite size may be the cause of this increase in the optical band gap of the samples. Because MgO has a lower electron affinity than ZnO, it contributes more electrons, which can be found at a higher Fermi level in Mg-doped ZCFAO samples. As a result, the radiative recombination of these excitons may result in a blue shift. The result is also similar to the reported results [41]. The rise in optical band with the Mg content indicates that the $Zn_{0.3-x}Mg_xCu_{0.7}Al_{0.3}Fe_{1.7}O_4$ samples are a suitable material for possibility optoelectronics devices having a large band gap. The extinction coefficient (k) depends on the density of free electrons and the structural defects in the sample; k can be expressed as [42]:

$$k = \alpha\lambda/4\pi \tag{5}$$

Figure 5 shows the relation between k and the wavelength (λ) where k declines with increasing Mg but rises with increasing λ. The alternation in the extinction coefficient may be due to the changes in the absorption process because of the presence of free carriers or not [43]. The characteristic property of the material, which determines the speed of light in that medium, is known as refractive index (n). The refractive index (n) of a material is a property that determines the light speed in that medium. The value of n was calculated using the following equations:

$$R = \frac{(n-1)^2 + k^2}{(n+1)^2 + k^2} \tag{6}$$

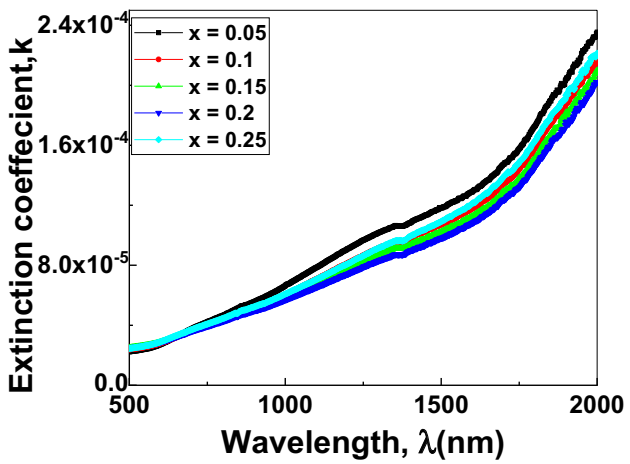

Fig. 5 Dependence of extinction coefficient on wavelength

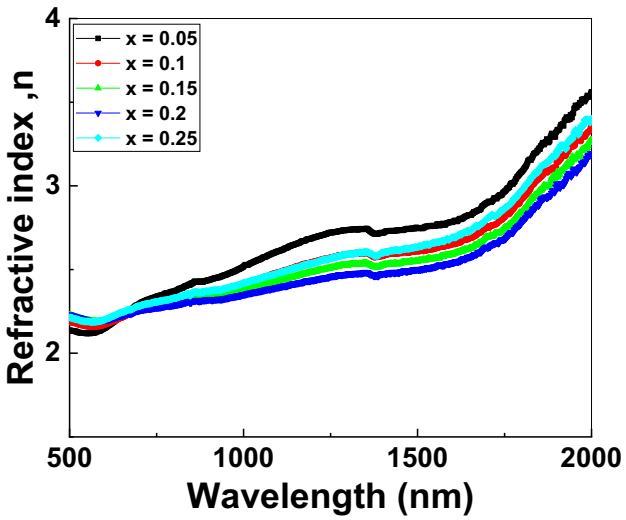

Fig. 6 Variation the refractive index with wavelength

$$n = \frac{(1+R)}{(1-R)} + \sqrt{\frac{4R}{(1-R)^2} - k^2} \tag{7}$$

The variation of n with (λ) is seen in Fig. 6. The variations in refractive index increase and decrease can be attributed to changes in the polarizability of constituent ions in the doped ZCFAO [43].

3.3 Dielectric Properties

3.3.1 Dielectric Constant

A non-destructive technique for determining the relationships between dielectric properties, structure, and microstructure is complex impedance spectroscopy. During the measurement procedure utilizing this technique, four variables were kept as a function of frequency: the dielectric loss, the phase angle, and the real and imaginary components of the impedance. The dielectric constant vaslues calculated using the following formula:

$$\varepsilon\prime = Cd/A\varepsilon_0 \tag{8}$$

where d is the thickness, is the surface area of the pellet, and ε_0 is the dielectric permittivity of free space.

Figure 7 depicts an example of the examined compounds $Zn_{0.25}Mg_{0.05}Cu_{0.7}Al_{0.3}Fe_{1.7}O_4$ dielectric constant dependence on applied frequency at a few selected temperatures. It is evident that ε′ is extremely large at lower frequencies, dramatically decreases with increasing frequency in the frequency range of 10 Hz to 10^3 kHz, diminishes slowly with raising frequency in the frequency region of 10^3 kHz to

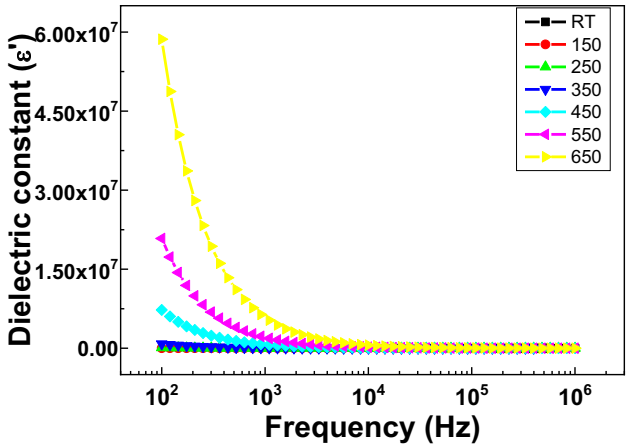

Fig. 7 Variation of dielectric constant (ε′) vs. frequency of $Zn_{0.25}Mg_{0.05}Cu_{0.7}Fe_{1.7}Al_{0.3}O_4$

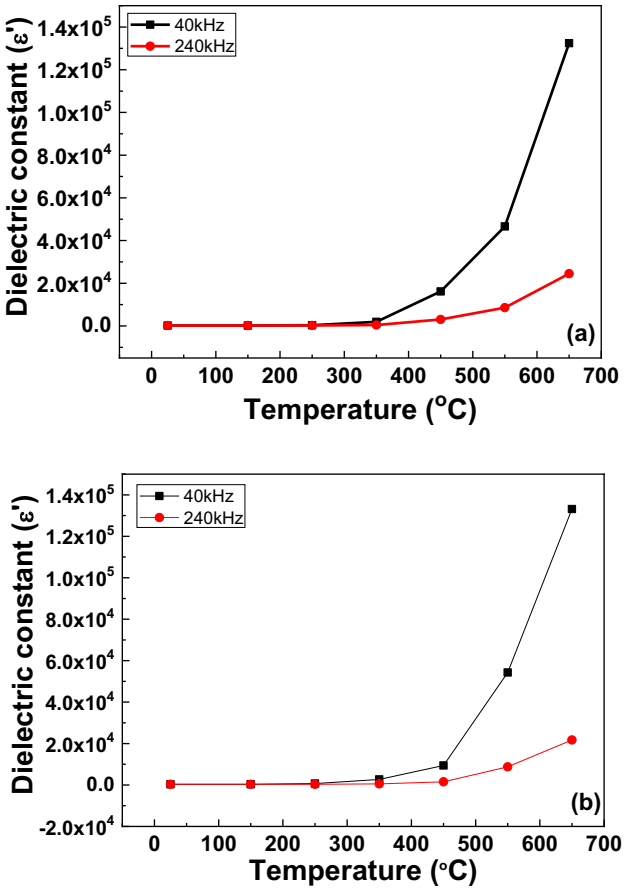

Fig. 8 **a**, **b** The variation of dielectric constant (ε′) with temperature at two chosen frequencies for the samples **a** $Zn_{0.25}Mg_{0.05}Cu_{0.7}Fe_{1.7}Al_{0.3}O_4$, **b** $Zn_{0.1}Mg_{0.2}Cu_{0.7}Fe_{1.7}Al_{0.3}O_4$

10^4 Hz, and essentially remains constant after 10^4 Hz [44]. Four types of polarizations-atomic, electronic, ionic, and interfacial—can be used to explain variations in dielectric permittivity with frequency [45]. All types of polarization contribute to the high dielectric constant at low frequencies, but interfacial polarization is more pronounced. Hoping electrons cannot cross highly resistant grain borders in the low frequency range, thus they cluster there and displace nearby charges, resulting in polarization at grain boundaries. At the grain-to-grain interface, Charges build up and create a thin layer. This layer's thickness is inversely correlated with capacitance (C = 1/d). As a result, a thin layer has a high dielectric constant. This is a common behavior of ferromagnetic materials, which Maxwell–Wagner model and Koop's hypothesis [46] indicate may be caused by interfacial polarization. The Maxwell–Wagner model states that ferrites have a two-layer dielectric structure. Large conducting grains make up the first layer, whereas poorly conducting grain boundaries make up the second layer (highly resistive). Grain boundaries contribute more significantly to dielectric polarization in low frequency regions. At grain boundaries, charges accumulate to form a thin layer of charges. At lower frequencies, the polarization of space charges caused by this thin layer of charges results in a high dielectric constant. Charges acquire enough energy to cross resistive grain boundaries as frequency rises. Charges conduct via bulk conducting grain and transcend grain boundaries. Low dielectric constant values are the result of a decrease in space charge polarization [47, 48]. This frequency dependence behavior can be explained by polarization process results from the random distribution of electrons across crystallographically equivalent locations among the ions of the same element, each of which has various valence states. In this instance, the electron exchange between Fe^{2+} and Fe^{3+} at the octahedral location is the main cause of the polarization process. In the low-frequency region, the electron hopping frequency between Fe^{2+} and Fe^{3+} is larger than the applied AC field. This makes the dipole more likely to interact with the applied field, increasing the dielectric constant. Due to electronic polarization, the dielectric constant stays constant as frequencies rise. The exchange of electrons between Fe^{2+} and Fe^{3+} ions during electronic polarization does not adhere to the variant high frequency alternating field. As a result, the dielectric constant gradually decreases and eventually becomes constant at higher frequencies [49].

3.3.2 Effect of Temperature on Dielectric Constant

Figure 8a and b depicts the variation of dielectric properties with temperature at two chosen frequencies. It is clearly that ε′ rises with increasing temperature. Due to the connection between orientational polarization and molecular thermal motion, dipoles cannot orient themselves under a changing electric field at low temperatures. It is nearly always found constant at low temperatures. With rising temperatures, dipoles become easier to orient, which raises the

orientational polarization value and ultimately causes the dielectric constant to rise with temperature [50].

3.3.3 Dielectric Loss

The phase difference between the applied alternating field and the induced current is represented by the angle δ in the dielectric loss tangent (tan δ). It is the ratio of energy loss to total stored energy in dielectric material. It is the energy loss in ferrite materials. Figure 9a–c makes it evident that as frequencies increase, tangent loss diminishes. Low-frequency tangent loss values are caused by highly resistive intergrain borders or grain–grain contact. High resistance had seen at grain–grain interfaces and intergrain borders limits the electrical exchange of Fe^{3+} and Fe^{2+}. As a result, electron hopping requires more energy, which raises tangent losses in the low frequency band. Conducting grain becomes more important at higher frequencies, and the amount of energy required for electronic hopping between Fe^{3+} and Fe^{2+} at the octahedral B site decreases. Therefore, in a high frequency range, energy losses are small. Also from this figure it is clear that tan δ increases with increasing temperature and this can be ascribed to the dissipation of the thermal energy due to thermal agitation.

3.3.4 Modulus and Impedance Spectroscopy

Figure 10 indicates the behaviors of real part of modulus (M) for $Zn_{0.25}Mg_{0.05}Cu_{0.7}Al_{0.3}Fe_{1.7}O_4$ vs. frequency and different temperatures. It is worth noting that in the low-frequency range, the real part of modulus (M′) exhibits very small values, which confirms that electrode polarization has a negligible impact on the materials [49–51]. However, as frequency increases, M′ values show a continuous rise and eventually tend to saturate at a maximum asymptotic value in the high-frequency range. This behavior might be due to the short-range mobility of charge carriers [45–48].

At all temperatures, the imaginary component of modulus exhibits a peak maxima centered at the M′ (ω) dispersion area (Fig. 11); as temperature increases, these maxima shift towards higher frequencies, as seen in Fig. Moreover, the range where the charge carriers were movable over extended distances is linked to the extent to the left of the peak maxima. On the other hand, the range where the charge carriers were limited to their potential barriers is connected to the area to the right of the maxima. They thereby demonstrated short-range mobility when an applied AC field was present.

The frequency of the peak maxima indicates the change in mobility from long-range to short-range. Additionally, the peak broadens with frequency at all temperatures, suggesting the presence of thermal activation of charge carriers with a relaxation time distribution and the contribution of both the bulk and temperature-dependent material

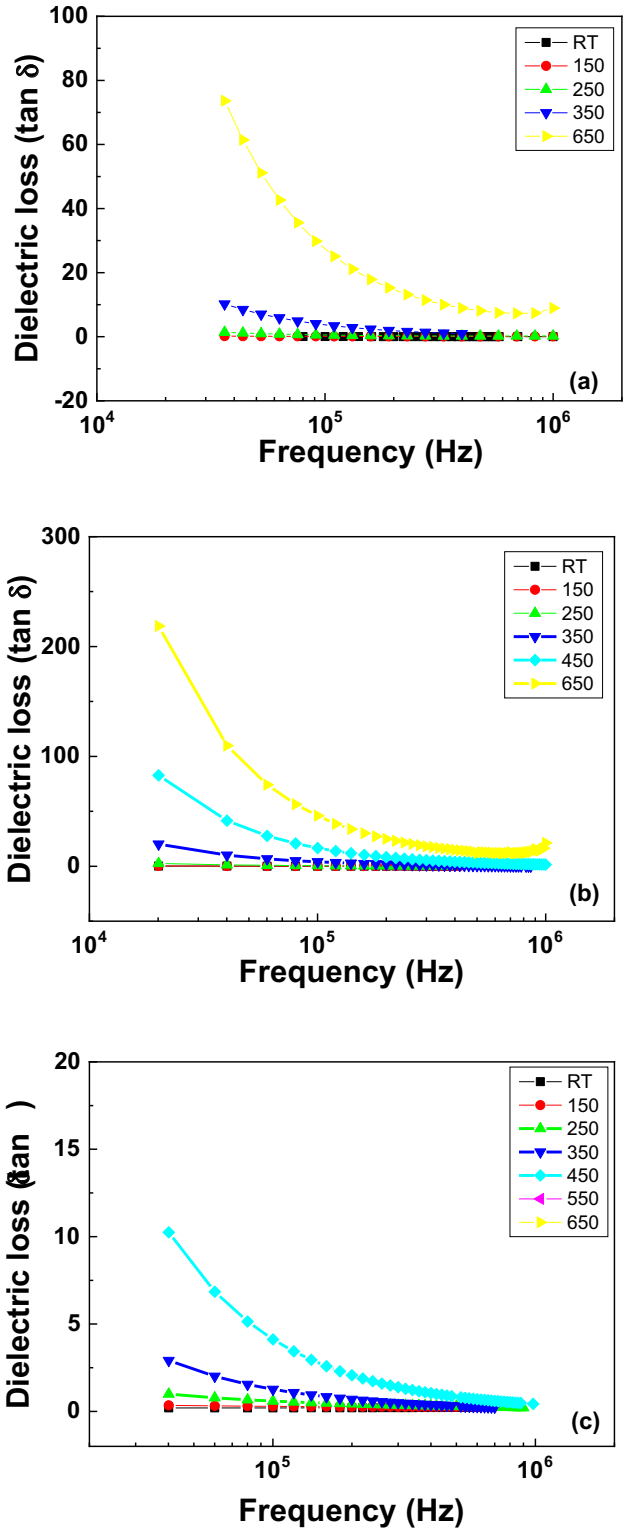

Fig. 9 **a–c** Variation of dielectric loss tangent (tan δ) with frequencies for the samples **a** $Zn_{0.25}Mg_{0.05}Cu_{0.7}Fe_{1.7}Al_{0.3}O_4$, **b** $Zn_{0.15}Mg_{0.15}Cu_{0.7}Fe_{1.7}Al_{0.3}O_4$, **c** $Zn_{0.05}Mg_{0.25}Cu_{0.7}Fe_{1.7}Al_{0.3}O_4$

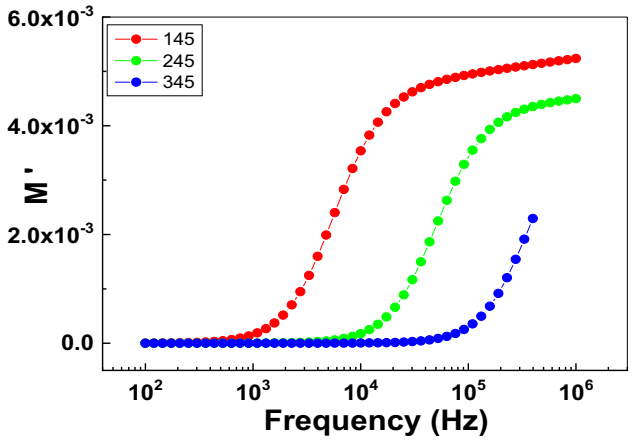

Fig. 10 The real part of modulus (M) for the sample $Zn_{0.25}Mg_{0.05}Cu_{0.7}Al_{0.3}Fe_{1.7}O_4$ vs. frequency at selected temperatures

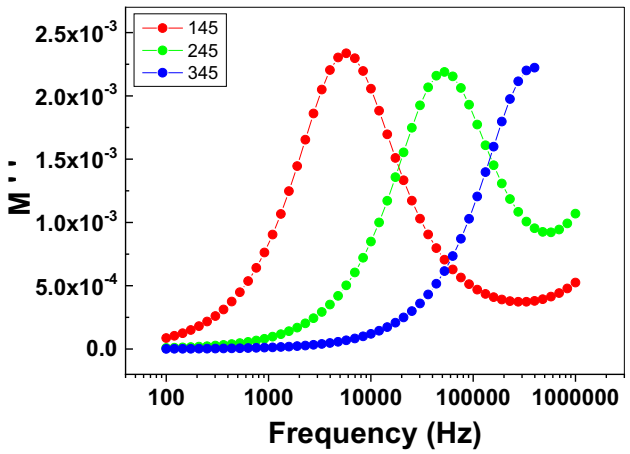

Fig. 11 The imaginary component of modulus versus frequency at selected temperatures for the sample $Zn_{0.25}Mg_{0.05}Cu_{0.7}Al_{0.3}Fe_{1.7}O_4$

interface to conductivity. In the electrical conduction of $Zn_{0.25}Mg_{0.05}Cu_{0.7}Al_{0.3}Fe_{1.7}O_4$, the overall behavior of frequency-dependent M″ clearly indicates the presence of a temperature-dependent hopping mechanism of charge transport phenomena [52].

The contribution to several relaxation processes, including electrode conduction, grain boundary, and grain, will be investigated by the examination of Nyquist plots of impedance. Nyquist plots between the Z″ and Z″ as a function of frequency at various temperatures are shown in Fig. 12. Semicircles with deviations in the low- and high-frequency zones have been the outcome of every plot. The semicircle's intercept at a lower Z value indicates both the grain boundary and the total resistance of the grain, whereas the intercept at a higher frequency indicates solely the resistance of the grain. This semicircle's diameter and grain resistance are correlated [53]. Semicircle diameters typically vary

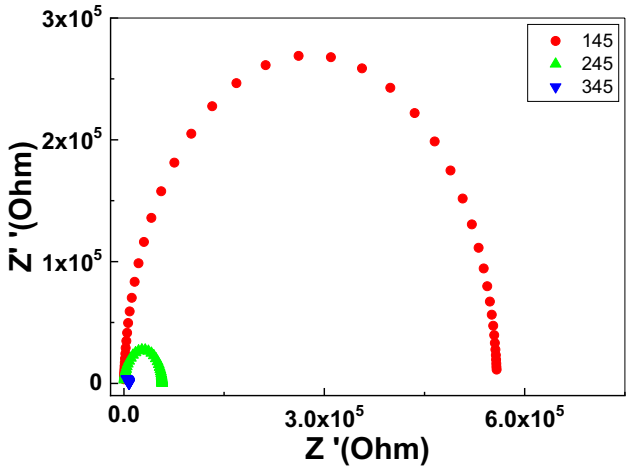

Fig. 12 Temperature dependent Nyquist plot for $Zn_{0.25}Mg_{0.05}Cu_{0.7}Fe_{1.7}Al_{0.3}O_4$

with doping, signifying a shift in the internal resistance of the grain. The resistance of the grain and grain boundaries are represented, respectively, by the diameter of semicircular arcs. High densities of imperfection seen in resistive intergrain boundaries prevent charge carriers from jumping along with the quickly changing AC field. Consequently, at lower frequencies, when resistive grain boundaries predominate, charge carriers relax. Resistive intergrain boundaries equate to a semicircle at low frequencies. The conducting grains are represented by a semicircle or semicircular arc at a high frequency with a low resistance value. Figure 12 clarifies that the produced doped compositions only show single semicircular arcs. This demonstrates the intergrain boundaries' predominant role in impedance. Nyquist graphs at fixed frequencies that are dependent on temperature are shown in Fig. 11. As temperature rises, the radius of semicircles and semicircular arcs decreases, indicating a drop in resistance and an increase in conduction at higher temperatures [54–56].

3.4 Magnetic Properties

For different ZCFAO samples recorded at ambient temperature, the magnetic hysteresis curves that trace the variation of the magnetization M as a function of the applied magnetic fields H are displayed in Fig. 13, where the applied fields extend to 2×10^3 G. The narrow hysteresis loops are observed, indicating that these ferrites have a soft magnetic nature. The coercive field H_c, remanent magnetization (M_r), and saturation magnetization (M_s) were determined using these curves; all of the data are reported in Table 2. From the extrapolation of the M_s vs. 1/H curves to 1/H−0, values of the saturation magnetization M_s for the samples were determined.

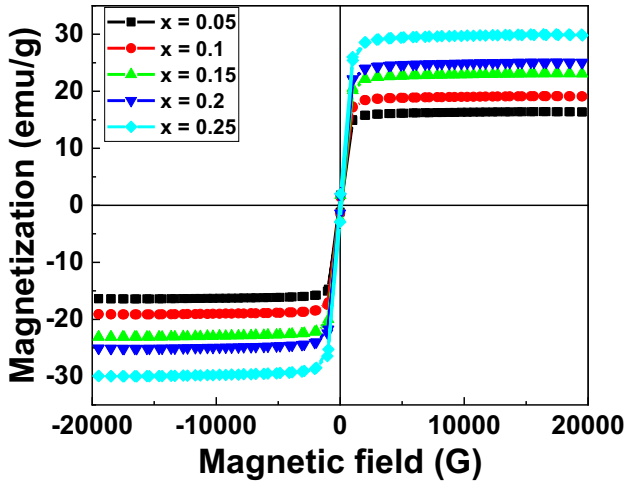

Fig. 13 Magnetic hysteresis loop of $Zn_{0.3-x}Mg_xCu_{0.7}Al_{0.3}Fe_{1.7}O_4 (0.05 \le x \le 0.25)$

The samples under investigation had low coercivity values, suggesting that they are members of the soft ferrite family. Up to 50 G, the samples' magnetization grows linearly with increasing applied magnetic field; above this field, the magnetization reaches maximum values before reaching saturation. It is observed that saturation magnetization increases linearly with increase in Mg content Fig. 14; this behavior can be understood as follow, through the intermediate O^{2-}anions and the superexchange mechanism, Three types of magnetic interactions between metallic ions have been identified: A–A, B–B, and A–B interactions exists, with the strongest exchange interaction being AB [57]. Consequently, the difference between the magnetic moments of the A (tetrahedral) and B (octahedral) sub-lattices yields the net magnetic moment and as we see from the cation distribution published before that [32]

Table 2 Saturation magnetization, coericivity, remanent magnetization, anisotropic constant and Squarness for the samples $Zn_{0.3-x}Mg_xCu_{0.7}Al_{0.3}Fe_{1.7}O_4$ $(0.05 \le x \le 0.25)$

Mg content, x	Saturation magnetization (emu/g)	Coericitivity (G)	Remanent magnetization (emu/g)	Anisotrpic constant	Squarness
0.05	16.416	77.149	1.2601	1319.2479	0.076
0.1	19.143	54.816	1.0112	1093.0653	0.052
0.15	23.103	57.721	1.2786	1389.0919	0.055
0.2	25.107	47.283	1.1022	1236.5982	0.043
0.25	29.983	51.639	1.4335	1612.8043	0.047

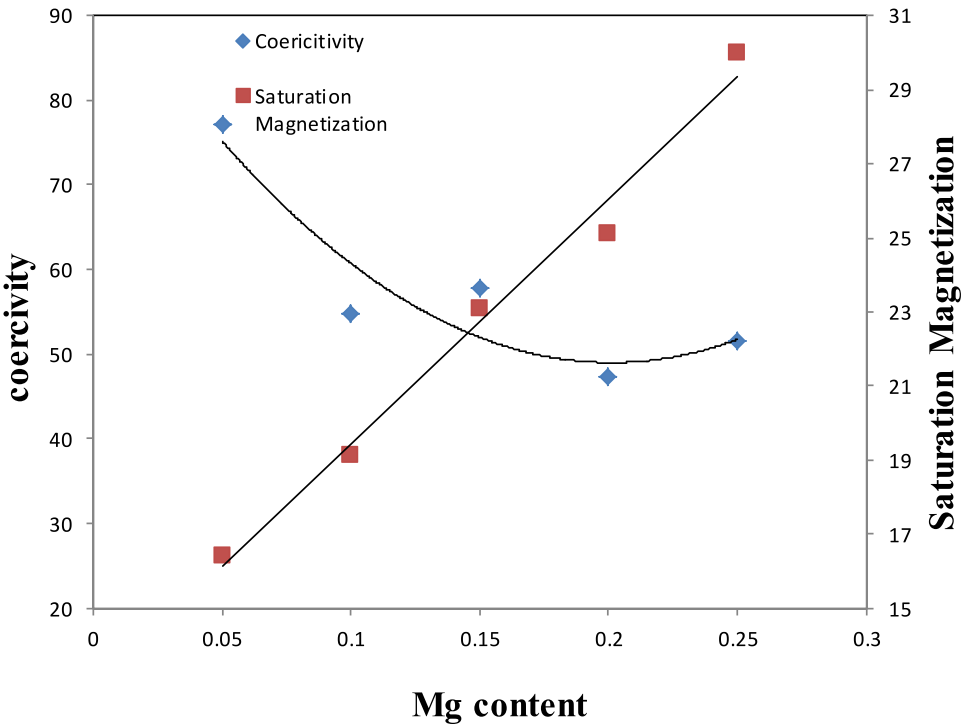

Fig. 14 Coercivity and saturation magnetization versus Mg content for $Zn_{0.3-x}Mg_xCu_{0.7}Al_{0.3}Fe_{1.7}O_4$ $(0.05 \le x \le 0.25)$

$x = 0.05 : \left[Zn_{0.25}Mg_{0.05}Cu_{0.133}Fe_{0.567}\right]A\ \left[Cu_{0.567}Fe_{1.33}Al_{0.3}\right]B_2O_4$

$x = 0.10 : \left[Zn_{0.20}Mg_{0.1}Cu_{0.2049}Fe_{0.4951}\right]A\ \left[Cu_{0.4951}Fe_{1.2049}Al_{0.3}\right]B_2O_4$

$x = 0.15 : \left[Zn_{0.15}Mg_{0.15}Cu_{0.25}Fe_{0.45}\right]A[Cu0.44Fe1.25Al0.3]B_2O_4$

$x = 0.20 : \left[Zn_{0.1}Mg_{0.2}Cu_{0.399}Fe_{0.301}\right]A\ \left[Cu_{0.301}Fe_{1.399}Al_{0.3}\right]B_2O_4$

$x = 0.25 : \left[Zn_{0.05}Mg_{0.25}Cu_{0.5174}Fe_{0.1826}\right]A\ \left[Cu_{0.1826}Fe_{1.574}Al_{0.3}\right]B_2O_4$

as the Mg content increases from 0.05 up to 0.25 the degree of inversion decreases which indicates that more Fe^{3+} cations with larger magnetic moment 5 Bohr magneton occupying the B sites and the A sites occupied by the diamagnetic cations Mg, Zn as well as the paramagnetic cations Cu^{1+} with 1 Bohr magneton so that AB exchange interaction (magnetic moment of B-A sublattices) with larger magnetic moment predominates and increases as the Mg content increases. The values of the anisotropic constant calculated using the next [58] relation and tabulated in Table 2

$$K1 = \left(M_s x Hc\right)/0.98 \tag{9}$$

where M_s is the saturation magnetization and H_c is the coercive force, from these values it is clear that the anisotropic constant enhanced with increasing both of the Mg content and saturation magnetization which reflects the anisotropy of the samples. From Table 2 it is also clear that the squareness ratio M_r/M_s decreases with increasing Mg content and it was found to be less than 0.5 for all samples indicate that the samples display single domain particles. Inspecting Fig. 14 when Mg cations enhanced, magnetic coercivity generally tends to decrease. The temperature, size, shape, microstrain, magnetocrystalline anisotropy, and inter-particle interaction of the particles all have a major impact on their magnetic coercivity [36]. Finally, these solid-state synthesized materials may reexamine the mechanisms underlying Mg^{2+} induced cationic exchange in ZCFAO and have prospective uses as soft-magnetic materials.

4 Conclusion

We have doped Mg ZCFAO ($Zn_{0.3-x}Mg_xCu_{0.7}Al_{0.3}Fe_{1.7}O_4$ ($0.05 \le x \le 0.25$)) spinel samples papered by solid State reaction at 1000 °C. X-ray diffraction studies proved the single phase cubic spinel structure related to the space group Fd-3m. Replacing Zn by Mg leads to an increase in the unit cell dimension due to the difference in the ionic radii. The degree of inversion as well as the crystallite size and lattice defects (dislocation density) was found to dominate with increasing the Mg content. The diminution in the crystallite size also may be due to the latent heat that had been trapped at the surface released, raising the local temperature and delaying development. The specific surface area was found to enhance due to a decrease in crystallite size and dislocations density in the order of 10^{-5} which reveal improving and completing the crystallization of the ferrite samples. The optical properties revealed that the band gap increases from 3.21 to 3.38 eV for the doped ZCFAO. The dielectric properties indicated that the dielectric constant ε′ was found to diminish with raising applied frequency. This is a common behavior of ferromagnetic materials, which Maxwell–Wagner model and Koop's hypothesis indicate may be caused by interfacial polarization. The dielectric constant increases with increasing temperature because with increasing temperature the dipoles become easier to orient, which raises the orientational polarization value and ultimately causes the dielectric constant to rise with temperature. Dielectric loss tangent (tan δ) was found to decline with raising frequency and boost with increasing temperature, this increase with temperature can be ascribed to the dissipation of the thermal energy due to thermal agitation. Using Nyquist diagram modeling, the sample impedance characteristics were interpreted while taking grain and grain boundary contributions into account. The magnetic characteristics demonstrated that the Mg^{2+} doped ZCFAO exhibit typical ferromagnetic behavior. The saturation magnetization increases with increasing Mg content as a result of cationic redistribution due to doping. The samples under investigation had low coercivity values, suggesting that they are members of the soft ferrite family. The magnetic coercivity tends to decrease with increasing Mg content. The squareness ratio M_r/M_s indicates that the samples display single domain particles.

Due to the main problem facing the world now being climate change, and this will push us to try to find a solution for this problem in our future work, by preparing a copper ferrite doped with different element in nanoparticle form using either sol–gel or autocombsion methods to be used in the applications for wastewater treatment and photocatalyst.

Author contributions A. M. Moustafa Performed the Sample Preparation, Conceptualization, Methodology, Data curation, Writing - review & editing, S. A. Gad Methodology, Data curation, Writing - review &

editing. , H. M. Hashem Conducted Formal Analysis and Investigation, review & editing. All authors have read and agreed to the published version of the manuscript.

Funding Open access funding provided by The Science, Technology & Innovation Funding Authority (STDF) in cooperation with The Egyptian Knowledge Bank (EKB).

Declarations

Competing interests The authors declare no competing interests.

References

1. R.S. Yadav, I. Kuřitka, J. Vilcakova, J. Havlica, J. Masilko, L. Kalina, J. Tkacz, M. Hajdúchová, V. Enev, Structural, dielectric, electrical and magnetic properties of $CuFe_2O_4$ nanoparticles synthesized by honey mediated sol–gel combustion method and annealing effect. J. Mater Sci. (2017). https://doi.org/10.1007/s10854-016
2. S. Rather, H.S. Bamufleh, H. Alhumade, A.A. Taimoor, U. Saeed, A.A. Al-Zahrani, O.M. Lemine, Morphological, structural, surface, thermal, chemical, and magnetic properties of Al-doped nanostructured copper ferrites. Ceram. Int. **49**(12), 20261–20272 (2023). https://doi.org/10.1016/j.ceramint.2023.03.149
3. A.R. Tehrani-Bagha, M. Gharagozlou, F. Emami, Catalytic wet peroxide oxidation of a reactive dye by magnetic copper ferrite nanoparticles. J. Environ. Chem. Eng. **4**, 1530–1536 (2016). https://doi.org/10.1016/j.jece.2016.02.014
4. Y. Fu, Q. Chen, M. He, Y. Wan, X. Sun, H. Xia, X. Wang, Copper ferrite-graphene hybrid: a multifunctional heteroarchitecture for photocatalysis and energy storage. Ind. Eng. Chem. Res. **51**, 11700–11709 (2012). https://doi.org/10.1021/ie301347j
5. J.A. Gomes, M.H. Sousa, G.J. da Silva, F.A. Tourinho, J. Mestnik-Filho, R. Itri, G.M. de Azevedo, J. Depeyrot, Cation distribution in copper ferrite nanoparticles of ferrofluids: a synchrotron XRD and EXAFS investigation. J. Magn. Magn. Mater. **300**, e213–e216 (2006). https://doi.org/10.1016/j.jmmm.2005.10.083
6. M. Kamran, M. Anis-ur-Rehman, Study of dielectric and electrical properties in Co-(Fe–Ce-Nd) nanosized spinel ferrites. Mater. Sci. Semicond. Process. **153**, 107111 (2023). https://doi.org/10.1016/j.mssp.2022.107111
7. A.M. Moustafa, I.S. AhmedFarag, M.H. Abdellatif, M.A. Ahmed, Structural analysis and role of cation distribution on the magnetic properties of single phase Ni-doped copper chromium ferrite. J. Mater Sci. **22**, 20099–20108 (2019). https://doi.org/10.1007/s10854-019-02384-9
8. M.A. Munir, M.Y. Naz, S. Shukrullah, M.U. Farooq, K. Kamran, M. Irfan, A.A.J. Ghanim, Testing of magnetic and dielectric traits of microwave plasma treated NiCuZn spinel ferrites for efficient energy storage and high-frequency applications. Mater. Sci. Eng. B (2023). https://doi.org/10.1016/j.mseb.2023.116374
9. N. Acharya, R. Sagar, Comparitive study on structure, dielectric and electrical properties of cobalt- and zinc-substituted Mn_3O_4 spinels. Appl. Phys. A **126**, 515 (2020). https://doi.org/10.1007/s00339-020-03659-3
10. N. Acharya, R. Sagar, Influence of frequency on dielectric and electrical behavior of $ZnMn_2O_4$. Mater. Today Proc. **27**, 382–384 (2020). https://doi.org/10.1016/j.matpr.2019.11.206
11. R. Sultana, G. Gurjar, S. Patnaik, V.P.S. Awana, Growth, characterization and high-field magneto-conductivity of $Co_{0.1}Bi_2Se_3$ topological insulator. J. Supercond. Nov. Magn. **32**, 769–777 (2019)
12. A.D. Korkmaz, S. Güner, Y. Slimani, H. Gungunes, Md. Amir, A. Manikandan, A. Baykal, Microstructural, optical, and magnetic properties of vanadium-substituted nickel spinel nanoferrites. J. Supercond. Nov. Magn. **32**, 1057–1065 (2019). https://doi.org/10.1007/s10948-018-4793-6
13. S. Yuvaraj, R.K. Selvan, Y.S. Lee, An overview of AB2O4- and A2BO4-structured negative electrodes for advanced Li-ion batteries. RSC Adv. **6**, 21448–21474 (2016). https://doi.org/10.1039/C5RA23503K
14. S.D. Sartale, C.D. Lokhande, M. Muller, Electrochemical synthesis of nanocrystalline $CuFe_2O_4$ thin films from non-aqueous (ethylene glycol) medium. Mater. Chem. Phys. **80**, 120–128 (2003). https://doi.org/10.1016/S0254-0584(02)00462-5
15. Z. Sun, L. Liu, D.Z. Jia, W. Pan, Simple synthesis of $CuFe_2O_4$ nanoparticles as gas sensing materials. Sens. Actuators B **125**, 144–148 (2007). https://doi.org/10.1016/J.SNB.2007.01.050
16. K.S. Kang, C.-H. Kim, W.-C. Cho, K.-K. Bae, S.-W. Woo, C.-S. Park, Reduction characteristics of $CuFe_2O_4$ and Fe_3O_4 by methane; CuFe2O4 as an oxidant for two-step thermochemical methane reforming. Int. J. Hydrogen Energy **33**, 4560–4568 (2008). https://doi.org/10.1016/j.ijhydene.2008.05.054
17. S. Kameoka, T. Tanabe, A.P. Tsai, Self-assembled porous nanocomposite with high catalytic performance by reduction of tetragonal spinel $CuFe_2O_4$. Appl. Catal. A **375**, 163–171 (2010). https://doi.org/10.1016/j.apcata.2009.12.035
18. N. Nasrallah, M. Kebir, Z. Koudri, M. Trari, Photocatalytic reduction of Cr(VI) on the novel hetero-system $CuFe_2O_4$/CdS. J. Hazard. Mater. **185**, 1398–1404 (2011). https://doi.org/10.1016/j.jhazmat.2010.10.061
19. R.K. Selvan, N. Kalaiselvi, C.O. Augustin, C.H. Doh, C. Sanjeeviraja, $CuFe_2O_4$/SnO_2 nanocomposites as anodes for Li-ion batteries. J. Power Sources **157**, 522–527 (2006). https://doi.org/10.1016/j.jpowsour.2005.07.030
20. S. Roy, J. Ghose, Mössbauer study of nanocrystalline cubic $CuFe_2O_4$ synthesized by precipitation in polymer matrix. J. Magn. Magn. Mater. **307**, 32–37 (2006). https://doi.org/10.1016/j.jmmm.2006.03.036
21. R.K. Selvan, C.O. Augustin, L.J. Berchmans, R. Saraswathi, Combustion synthesis of $CuFe_2O_4$. Mater. Res. Bull. **38**, 41–54 (2003). https://doi.org/10.1016/S0025-5408(02)01004
22. M. Sultan, R. Singh, Magnetization and crystal structure of RF-sputtered nanocrystalline $CuFe_2O_4$ thin films. Mater. Lett. **63**, 1764–1766 (2009). https://doi.org/10.1016/j.matlet.2009.05.027
23. F.A. Abuilaiwia, M. Awaisc, U.Y. Qazia, F. Alie, A. Afza, Al^{3+} doping reduces the electron/hole recombination in photoluminescent copper ferrite ($CuFe_{2-x}Al_xO_4$) nanocrystallites. Boletín de la Sociedad Española de Cerámica y Vidrio **61**, 252–262 (2022). https://doi.org/10.1016/j.bsecv.2020.11.007
24. S. Akhter, D.P. Paul, S. Akhter, D.K. Saha, S.M. Hoque, M.A. Hakim, Structural, magnetic and electrical properties of Cu–Mg ferrites. Sci. Res. **6**(2), 205–215 (2014). https://doi.org/10.3329/jsr.v6i2.17351

25. S. Akhter, D.P. Paul, M.D. AbdulHakim, D.K. Saha, M.D. Al-Mamun, A. Parveen, Synthesis, structural and physical properties of $Cu_{1-x}Zn_xFe_2O_4$ ferrites. Mater. Sci. Appl. **2**, 1675–1681 (2011). https://doi.org/10.4236/msa.2011.211223
26. S. Akter, M.N.I. Khan, F. Ferdous, H.N. Das, I.M. Syed, Analysis of the influence of trivalent Cr^{3+} doping on the structural and electromagnetic properties of $Cu_{0.5}Mg_{0.5}Cr_xFe_{2-x}O_4$ nanoferrites. AIP Adv. **12**, 095015 (2022). https://doi.org/10.1063/5.0110308
27. A.M. Moustafa, I.S. AhmedFarag, L.M. Salah, Structural characterization of substituted calcium titanate compounds $Ca_{1-X}La_XTi_{1-x}Fe_xO_3$. Egypt. J. Solids **27**(2), 213–222 (2004)
28. A.M. Moustafa, L.M. Salah, M. Salerno, M.H. Abdellatif, Symmetry in magnetic and vibrational spectra of multi-element spinel ferrite. J. Magn. Magn. Mater. **513**, 167267 (2020). https://doi.org/10.1016/j.jmmm.2020.167267
29. A.F. Hegab, I.S. AhmedFarag, A.M. EL-Shabiny, A.M. Nassaar, A.A. Ramadan, A.M. Moustafa, Role of Sr doping on transport and magnetic properties of bismuth ferrite in correlation with defect formation. J. Mater. Sci. **28**, 14460–14470 (2017). https://doi.org/10.1007/s10854-017-7308-5
30. T. Ungár, Microstructural parameters from X-ray difraction peak broadening. Scr. Mater. (2004). https://doi.org/10.1016/j.scriptamat.2004.05.007
31. M. Ashtar, A. Munir, M. Anis-ur-rehman, A. Maqsood, Effect of chromium substitution on the dielectric properties of mixed Ni–Zn ferrite prepared by WOWS sol–gel technique. Mater. Res. Bull. **79**, 14–21 (2016). https://doi.org/10.1016/j.materresbull.2016.02.044
32. I.S. AhmedFarag, M.A. Ahmed, S.M. Hammad, A.M. Moustafa, Study of cation distribution in $Cu_{0.7}(Zn_{0.3-x}Mg_x)Fe_{1.7}Al_{0.3}O_4$ by X-ray diffraction using Rietveld method Egypt. J. Sol. **24**, 215–225 (2001)
33. M.Z. Dang, D.G. Rancourt, J.E. Dutrizac, G. Lamarche, R. Provencher, Interplay of surface conditions, particle size, stoichiometry, cell parameters, and magnetism in synthetic hematite-like materials. Hyperfne Interact. **117**(1–4), 271–319 (1998). https://doi.org/10.1023/A:1012655729417
34. R.E. Elshater et al., Structural phase transition of spinel to hematite of as-prepared Fe^{2+}–Cr nanoferrites by sintering temperature. J. Int. Meas. Confed. **132**, 272–281 (2019). https://doi.org/10.1016/j.measurement.2018.09.021
35. R.E. El shater, A.W. Awad, E.K. Abdel Khalek, H.H. El Bahnasawy, T.M. Meaz, E.A. Okba, Infuence of sintering temperature on structural and optical properties of $Cd_{0.5}Cu_{0.5}Cr_xFe_{2-x}O_4$ ferrites. Sci. Rep. **13**, 15482 (2023). https://doi.org/10.1038/s41598-023-41214-1
36. U. Megha, G. Varghese, K. Shijina, Effect of Bi and Sr doping on morphological and magnetic properties of $LaCo_{0.6}Fe_{0.4}O_3$ nanosized perovskites. Bull. Mater. Sci. **39**, 125–131 (2016). https://doi.org/10.1007/s12034-015-1149-8
37. P.U. Aparna, N.K. Divya, P.P. Pradyumnan, Structural and dielectric studies of Gd doped ZnO nanocrystals at room temperature. J. Mater. Sci. Chem. Eng. **4**, 79–88 (2016). https://doi.org/10.4236/msce.2016.42009
38. S.A. Gad, A.M. Moustafa, A.A. Azab, A.F. Hegab, impact of chromium doping on structural, optical, magnetic and electrical properties of nano copper ferrite. J. Ovonic Res. **16**(5), 293–308 (2020)
39. J. Massoudi, M. Smari, K. Nouri, E. Dhahri, K. Khirouni, S. Bertaina, L. Bessais, E.K. Hlil, Magnetic and spectroscopic properties of Ni–Zn–Al ferrite spinel: from the nanoscale to microscale. RSC Adv. **10**, 34556 (2020). https://doi.org/10.1039/d0ra05522k
40. A.M. Moustafa, S.A. Gad, A.A. Ward, Impact of molybdenum doping on the structural, optical and dielectric properties of α-$A_{l2-x}Mo_xO_3$. ECS J. Solid State Sci. Technol. **10**, 043007 (2021)
41. J. Narayan, A.K. Sharma, A. Kvit, C. Jin, J.F. Muth, O.W. Holland, Novel cubic $Zn_xMg_{1-x}O$ epitaxial heterostructures on Si (100) substrates. Solid State Commun. **121**, 9 (2002). https://doi.org/10.1016/S0038-1098(01)00431-8
42. Q. Feng, T. Horiuchi, T. Mitsusio, K. Yanagisawa, N. Yamasaki, Hydrothermal soft chemical synthesis of NH+4 form of hollandite-type manganese oxide. J. Mater. Sci. Lett. **18**, 1375 (1999)
43. M.S. Dawood, T.A. Elmosalami, W.M. Desoky, Enhancement of elastic, optical and opto-electrical properties of Ni-Substituted $CoFe_2O_4$ nanoparticles with different concentrations. Opt. Mater. **117**, 111101 (2021). https://doi.org/10.1016/j.optmat.2021.111101
44. M. Kamran, M. Anis-ur-Rehman, Enhanced transport properties in Ce doped cobalt ferrites nanoparticles for resistive RAM applications. J. Alloys Compd. **822**, 153583 (2020). https://doi.org/10.1016/j.jallcom.2019.153583
45. A. Verma, R. Chatterjee, Effect of zinc concentration on the structural, electrical and magnetic properties of mixed Mn–Zn and Ni–Zn ferrites synthesized by the citrate precursor technique. J. Magn. Magn. Mater. **306**(2), 313–320 (2006). https://doi.org/10.1016/j.jmmm.2006.03.033
46. S.U. Haque, K.K. Saikia, G. Murugesan, S. Kalainathan, A study on dielectric and magnetic properties of lanthanum substituted cobalt ferrite. J. Alloys Compd. **15**(701), 612–618 (2017). https://doi.org/10.1016/j.jallcom.2016.11.309
47. S. Saha, T.P. Sinha, Low-temperature scaling behavior of $BaFe_{0.5}Nb_{0.5}O_3$. Phys. Rev. B. **65**, 1341 (2005)
48. K.P. Padmasree, D.D. Kanchan, A.R. Kulkami, Impedance and Modulus studies of the solid electrolyte system 20CdI2–80[$xAg_{2O-y}(0.7V_2O_5$–$0.3B_2O_3)$], where $1 \leq x/y \leq 3$. Solid State Ionics. **177**(5–6), 475–482 (2006). https://doi.org/10.1016/j.ssi.2005.12.019
49. A.K. Nikumbh, R.A. Pawar, D.V. Nighot, G.S. Gugale, M.D. Sangale, M.B. Khanvilkar, A.V. Nagawade, Structural, electrical, magnetic and dielectric properties of rare-earth substituted cobalt ferrites nanoparticles synthesized by the co-precipitation method. J. Magn. Magn. Mater **1**(355), 201–209 (2014). https://doi.org/10.1016/j.jmmm.2013.11.052
50. N. Shukla, V. Kumar, D.K. Dwivedi, Dependence of dielectric parammeters and A.C. conductivity on frequency and temperature in bulk $Se_{90}Cd_8In_2$ glassy alloy. J. Non-Oxide Glass. **8**(2), 47–57 (2016)
51. N.H. Vasoya, P.K. Jha, K.G. Saija, S.N. Dolia, K.B. Zankat, K.B. Modi, Electric modulus, scaling and modeling of dielectric properties for Mn^{2+}–Si^{4+} Co-substituted Mn–Zn Ferrites. J. Electron. Mater. **45**, 917–927 (2016). https://doi.org/10.1007/s11664-015-4224-4
52. M. Javed, A.A. Khan, M.S. Ahmed, S.N. Khisro, J. Kazmi, R. Bilkees, M.N. Khan, M.A. Mohamed, Temperature dependent impedance spectroscopy and electrical transport mechanism in sol–gel derived $MgCr_2O_4$ spinel oxide. Physica B **599**, 412377 (2020). https://doi.org/10.1016/j.physb.2020.412377
53. M. Kamran, M. Anis-ur-Rehman, Study of dielectric and electrical properties in Co–(Fe–Ce–Nd) nanosized spinel ferrites. Mater. Sci. Semi. Process. **153**, 107111 (2023). https://doi.org/10.1016/j.mssp.2022.107111
54. N. Acharya, R. Sagar, Structure and electrical properties characterization of $NiMn_2O_4$ NTC ceramics. Inorg. Chem. Commun. **132**, 108856 (2021). https://doi.org/10.1016/J.INOCHE.2021.108856
55. M.A. Dar, K.M. Batoo, V. Verma, W.A. Siddiqui, R.K. Kotnala, Synthesis and characterization of nano-sized pure and Al-doped lithium ferrite having high value of dielectric constant. J. Alloys Compd. **493**(1–2), 553–560 (2010). https://doi.org/10.1016/j.jallcom.2009.12.154
56. C. Murugesan, G. Chandrasekaran, Impact of Gd^{3+} substitution on the structural, magnetic, and electrical properties of cobalt ferrite nanoparticles. RSC Adv. **5**, 73714–73725 (2015). https://doi.org/10.1039/C5RA14351A
57. B. Viswanathan, V.R.K. Murthy, *Ferrite Materials: Science and Technology* (Narosa Pub House, Berlin, 1990)

58. J. Li, P. Jing, X. Zhang, D. Cao, J. Wei, L. Pan, Z. Liu, J. Wang, Q. Liu, Synthesis, characterization and magnetic properties of $NiFe_{2-x}Ce_xO_4$ nanoribbons by electrospinning. J. Magn. Magn. **425**, 37–42 (2017). https://doi.org/10.1016/j.jmmm.2016.10.113